



Theoretical and Finite Element Analysis of Static Friction Between Multi-Scale Rough Surfaces

Xianzhang Wang¹ · Yang Xu¹ · Robert L. Jackson¹

Received: 30 July 2018 / Accepted: 12 October 2018 / Published online: 25 October 2018
© Springer Science+Business Media, LLC, part of Springer Nature 2018

Abstract

The current work considers the multi-scale nature of roughness in a new model that predicts the static friction coefficient. This work is based upon a previous rough surface contact model, which used stacked elastic–plastic 3-D sinusoids to model the asperities at multiple scales of roughness. A deterministic model of a three-dimensional deformable rough surface pressed against a rigid flat surface is also carried out using the finite element method (FEM). The accuracy of the deterministic FEM model is also considered. At the beginning of contact, which is surface-point contact, the asperities or peaks are isolated, sharp, and the contact areas consist of an inadequate number of elements and sources of error. In this range of contact, the results are not presented as real or accurate. As the normal load increases, the number of the contact elements become larger, and thus, the results become more accurate. That is, the deterministic FEM results are most accurate at high loads. Spectral interpolation is used to smooth the geometry in between the original measured nodes. The effects of normal load and plasticity index on static friction are then analyzed. The results predicted by the theoretical model are also compared to other existing rough surface friction contact models and the FEM results. They are in a good qualitative agreement, especially for higher loads and higher plasticity indices. The FEM model also has significant error, but it is more accurate at higher loads where the proposed multi-scale static friction model and FEM model are in better agreement.

Keywords Contact mechanics · Static friction · Surface roughness analysis and models

Abbreviations

Nomenclature

A	Area of contact
A_0	Contact area under normal preload only
A_n	Nominal contact area of the surface
A_r	Real contact area
A_s	Contact area at sliding inception
C	Critical yield stress coefficient
E	Elastic modulus
E'	$E/(1-\nu^2)$
f	Spatial frequency (reciprocal of wavelength)
F	Contact force for single asperity

F_f	Friction force
F_n	Normal preload
F_n^*	Dimensionless normal preload
F_t	Tangential load
L	Scan length
N	Number of nodes
N_e	Number of elements
p^*	Average pressure to cause complete contact (Elastic)
p_{ep}^*	Average pressure to cause complete contact (Elastic–plastic)
\bar{p}	Average pressure over the entire surface
S_y	Yield strength
u_x	Displacement in the x direction

✉ Xianzhang Wang
xzw0011@auburn.edu

Yang Xu
yzx0007@auburn.edu

Robert L. Jackson
robert.jackson@eng.auburn.edu

¹ Mechanical Engineering Department, Auburn University, Auburn, AL 36849, USA

Greek symbols

λ	Asperity wavelength
Δ	Asperity amplitude
Δ_c	Critical asperity amplitude
ψ	Sinusoidal asperity parameter
Ψ	Plasticity index
σ	Standard derivation on the surface heights
σ_s	Standard derivation on the asperity heights

ν	Poisson's ratio
τ_c	Critical interfacial shear strength
ω_0	Interference under normal preload
ω_c	Critical interference (full stick condition)
ω_{cs}	Critical interference (perfect slip condition)
μ_s	Static friction coefficient
μ_s	Static friction coefficient

Subscripts

c	Critical value at the onset of plastic deformation (full stick condition)
ave	Average value
max	Maximum value
ep	Elastic–plastic
JGH	From model by Johnson, Greenwood, and Higgonson [1]
x	In the x direction

1 Background

Friction plays an important role in everyday life, especially for engineering components. Friction is the force resisting the relative motion of solid surfaces in contact sliding against each other. There are several types of friction; one of the most common type is dry friction. Dry friction arises from a combination of interface adhesion, surface roughness, surface deformation, and so on. The friction force required to start sliding is usually greater than the force required to maintain sliding, and this has given rise to the notion that there are two coefficients of friction: static (for the surfaces at rest) and kinetic (for surfaces in motion) friction coefficients.

The so-called laws of friction were provided by Amonton, although DaVinci may have also been responsible. Amonton's first law: the friction force, F_f , is directly proportional to the applied normal force, F_n . Amonton's second law: the friction force, F_f , is independent of the apparent area, F_n . Coulomb's law: kinetic friction is independent of sliding velocity.

Then, Euler summarized these laws and provided an equation:

$$F_f = \mu F_n \quad (1)$$

where μ is the coefficient of friction.

However, none of these 'laws' hold universally. While these laws provide a general guideline of the sensitivity of the coefficient of friction to the materials in contact, they may not necessarily be representative of friction that results between actual contact pairs [1]. From the second of Amonton's friction laws, friction is independent of apparent area of contact. Bowden and Tabor may have been the first to state that this was due to surface roughness. Although some surfaces look

very smooth, they are rough to some degree at the micro- or nanoscale. When two rough surfaces are pressed together, a contact is made by the asperities or peaks on either surface. These small asperity contacts make up the real contact area. For rough surfaces, the friction force becomes nearly independent of the nominal contact area, but proportional merely to the real contact area. Bowden and Tabor [2] later made a critical insight into the cause of friction and the physical reason behind the laws. They presented a different approach, which considered the sliding inception and static friction as a failure mechanism related to the material properties. They then assumed that when the sliding occurs the average shear stress over the real contact area of contact has the value of, τ_{ave} . The expression for the total friction force, F_f , then can be given as:

$$F_f = \tau_{ave} \cdot A_r \quad (2)$$

To understand the friction, it is important to understand the effect of surface morphology and load on the tribological performance of different rough surfaces. Hence, numerous models that predict the asperity-scale static friction were developed by many researchers [3–7]. This includes asperity contact under combined normal and tangential loads. For the rough surface contact, numerous studies were carried out on the pre-sliding static friction [8–11]. Most commonly, the roughness is considered using a statistical model [12]: This model incorporates the results of the finite element method and sliding inception of a single asperity in a statistical representation of the surface roughness.

In 1988, based on the principles of Tabor and Bowden [2], Chang, Etsion, and Bogy (CEB) [8] created one of the first elastic–plastic asperity contact models. They found the effect of normal load on the maximum tangential load is significant and included it in a statistical model of rough surface contact (Greenwood and Williamson (GW) [12]) by a collection of spherical asperities with a Gaussian height distribution, for which the asperity height probability density, $\phi(z)$, is given by:

$$\phi(z) = \frac{1}{\sqrt{2\pi}\sigma_s} \exp \left[-0.5 \left(\frac{z}{\sigma_s} \right)^2 \right] \quad (3)$$

where σ_s is the standard derivation on the asperity heights.

In the CEB model, the inception of slip of each asperity occurred at the first yielding (also yield inception) of the surface in contact (considering shear and normal load). Hence, the maximum tangential force that all the contacting asperities can support was assumed to be the static friction of the contacting rough surfaces, and it can be calculated by the von Mises criterion. The static friction coefficient is given in the form:

$$\mu_s = \frac{(F_t)_{\max}}{F_{\text{ext}}} = \frac{(F_t)_{\max}}{F_n - F_s} \quad (4)$$

where $(F_t)_{\max}$ is the tangential force needed to shear the junctions, F_n is the normal force, and F_s is the adhesion force.

Based on the analysis of metallic surfaces, the CEB work found that the smooth surfaces and the harder materials can support more shear force. In contrast, the static friction coefficient decreases as both the plasticity index and the dimensionless external force increase. The effect of small normal loads on the static friction coefficient was experimentally investigated, and it was confirmed that the static friction coefficient decreases as the normal load increases [13].

The FEM results of a single asperity contact can also be incorporated into a statistical model to represent the rough surfaces in the elastic–plastic or fully plastic regimes. Kogut and Etsion (KE) [9] present a model that incorporates the results of finite element results in [3] into a statistical representation of surface roughness. They suggest that the CEB failure criterion used in [8] underestimated the tangential force needed to shear the junctions, because the elastic region surrounding the single plastic spot can support additional tangential load. They analyzed the effects of the tangential force, nominal contact area, plasticity index, Ψ , and adhesion parameter, θ , on the static friction coefficient. Much later, Cohen et al. analyzed the static friction coefficient [10] and junction growth [14] in FEM under the full stick condition. They incorporated the finite element results [4] into a statistical representation of surface roughness to predict the static friction between rough surfaces. By using two of the same governing equations in the GW model, the normal load F_n and maximum friction force, $(F_t)_{\max}$, can be expressed as:

$$F_n = \eta A_n \int_{d^*}^{\infty} \bar{F}(\omega^*) \phi^*(z^*) dz^* \tag{5}$$

$$(F_t)_{\max} = \eta A_n \int_{d^*}^{\infty} (\bar{F}_t)_{\max}(\omega^*) \phi^*(z^*) dz^* \tag{6}$$

By solving Eq. (6) and finding a best fit curve to the results, the dimensionless static friction $(F_t)_{\max}^*$ is given by [10]:

$$(F_t)_{\max}^* = \left(0.26 + \frac{0.43}{\psi}\right) (F_n^*)^{(0.0095\psi+0.91)} \tag{7}$$

Hence, the static friction coefficient is given by [10]:

$$\mu_s = \frac{(F_t)_{\max}^*}{F_n^*} = \left(0.26 + \frac{0.43}{\psi}\right) (F_n^*)^{(0.0095\psi-0.09)} \tag{8}$$

where $(F_t)_{\max}^*$ is the dimensionless tangential load and given by:

$$F_n^* = \frac{(F_t)_{\max}}{A_n S_y} \tag{9}$$

F_n^* is the dimensionless normal load and given by:

$$F_n^* = \frac{F_n}{A_n S_y} \tag{10}$$

and the plasticity index, ψ , is given by:

$$\psi = \frac{2E'}{\pi C S_y} \sqrt{\frac{\sigma_s}{R}} \tag{11}$$

where σ_s is the standard deviation of the asperity heights and given by McCool [15] as

$$\sigma_s = \left(1 - \frac{0.8968}{\alpha}\right)^{0.5} m_0^{0.5} \tag{12}$$

C is given by [16]

$$C = 1.295 \exp(0.736 \nu) \tag{13}$$

α is the bandwidth parameter:

$$\alpha = \frac{m_0 m_4}{m_2^2} \tag{14}$$

The spectral moments m_0 , m_2 , and m_4 are the variance of heights, mean square slope, and the mean square concavity, respectively. They are all given by McCool [15] as

$$m_0 = \frac{1}{N} \sum_{n=1}^N [z(x)]_n^2 \tag{15}$$

$$m_2 = \frac{1}{N} \sum_{n=1}^N \left(\frac{dz}{dx}\right)_n^2 \tag{16}$$

$$m_4 = \frac{1}{N} \sum_{n=1}^N \left(\frac{d^2z}{dx^2}\right)_n^2 \tag{17}$$

The average asperity radius of curvature then can be given as

$$R = 0.375 \left(\frac{\pi}{m_4}\right)^{0.5} \tag{18}$$

However, the plasticity index is also dependent on multiple scales of roughness [17]. Jackson and Green [18] proposed an alternative formulation based on the multi-scale rough surface contact method (note that it is not equivalent to Eq. 10):

$$\psi = \frac{B_{\max}}{B_c} \quad (19)$$

However, the theoretical equation for static friction in Cohen et al. [10] is not valid for plasticity indices above 8. Li, Etsion, and Talke [11] extended the model to higher plasticity indices by incorporating the FEM results that considering the large (full plasticity) deformation of Jackson and Green [16]. The empirical expressions of plasticity values in the range of $0 < \psi \leq 32$, were derived [11]. The static friction coefficient is given by [11]:

$$\mu_s = \frac{(F_t)_{\max}^*}{F_n^*} = [0.26 + 0.32\exp(-0.34\psi^{1.19})] (F_n^*)^{-\exp(-1.9\psi^{0.4})} \quad (20)$$

Several experimental studies were performed by researchers. The effects of skewness and kurtosis on the original CEB statistical static friction model [8] were investigated by Tayebi and Polycarpou [19]. In 2007, Lee and Polycarpou [20] sought to verify the statistical-based static friction models by using a precision experimental apparatus. They made comparisons to the measurements using the static friction model derived by Kogut and Etsion [1], which also includes the effects of adhesion. Recently, Lee et al. [21] also examined the effect of non-Gaussian or asymmetric asperity height distributions on the statistical static friction models and compared the predictions to experimental measurements. They found that the model developed by Cohen et al. [10] predicts higher friction coefficients, and the model provided by Kogut and Etsion [1] with the Pearson distribution has a good agreement with the experimental results. Later, Ibrahim-Dickey et al. [22] used an experimental method to measure the static friction between tin surfaces. The experimental results have a reasonable qualitative agreement with the theoretical model given by Li et al. [11]. It should be noted, however, that in all of these papers the asperities were modeled as spheres.

Due to the multi-scale nature of rough surfaces, there are many other methods to model the contact of rough surfaces. Archard [23] developed probably the first multi-scale contact model between rough surfaces. The rough surfaces used in Archard's model are described as "protuberances on protuberances." By using a concept of multiple scales of the asperities, the model considers smaller spheres layered upon larger spheres. Ciavarella et al. [24] solved the contact problem of a 2D Weierstrass–Mandelbrot fractal surface in contact with a rigid flat using the same stacked asperity assumption. They modeled the surface deformation using the two-dimensional elastic sinusoidal solution given by Westergaard [25]. Jackson and Streater [26] also developed an elastic–plastic multi-scale rough surface contact model using the same layered asperity structure. In addition to their work, Gao and Bower [27] also extended the multi-scale stacked

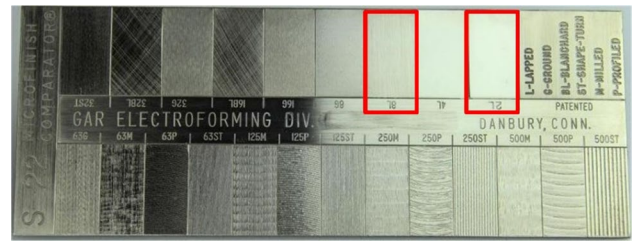


Fig. 1 S-22 micro-finish comparator surface finish scale



Fig. 2 NANOVEA ST400 optical profilometer

contact model by including plastic deformation for 2-D sinusoidal asperities. Based upon the model in [26], Wilson et al. [28] used stacked 3D elastic–plastic sinusoids to model the multiple scales of roughness. However, a multi-scale stacked model predicting the static friction between rough surfaces is still missing. Various theories and numerical models [26, 29–40] for the contact of rough surfaces were summarized and compared in [41], in which each approach was able to reproduce some of the reference solutions. This work focuses on the multi-scale stacked modeling and deterministic FEM modeling.

2 Rough Surfaces

2.1 Measured Real Surfaces

In this study, a standard micro-finish comparator was used for surface data (see Fig. 1). The micro-finish comparator contains machined surface finish specimens from different machining processes. The lapped surfaces 2L, 8L, and milled surface 63M were also measured and used in the FE model and theoretical analysis. A NANOVEA ST400 white

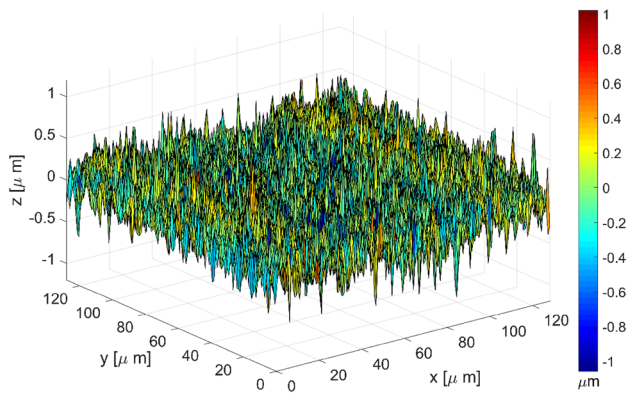


Fig. 3 Three-dimensional plot of the surface 2L

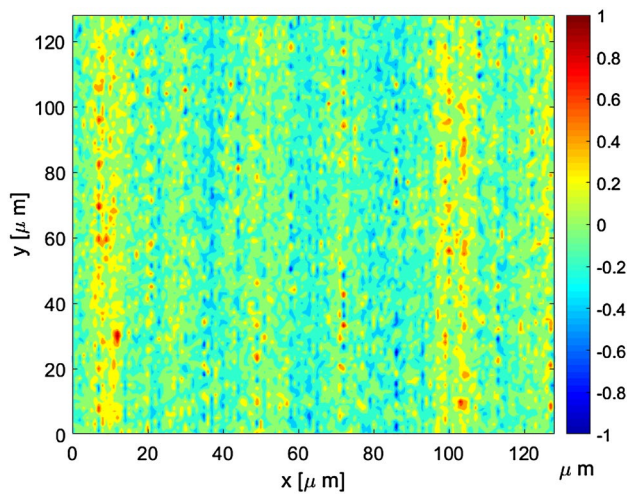


Fig. 4 Topographical contour plot of the surface 2L

light optical profilometer (see Fig. 2) is used to measure the real surfaces.

We first consider surface 2L. The surface height roughness is 0.204 μm . Its three-dimensional plot and contour are shown in Fig. 3. and Fig. 4, respectively.

2.2 Random Gaussian Rough Surface

In statistical contact models, the asperity heights of a rough surface are described by a Gaussian distribution, although in reality all engineering surfaces follow a non-Gaussian distribution. Note that surface height, z , and asperity height, z_s , are

different. The surface heights are the data collected from a profilometer, whereas asperity heights are calculated from the definition of the asperity, which is the surface points taller than their surrounding points. As suggested in [21, 42, 43], it is reasonable that the surface height and asperity height have similar behaviors.

In order to do an effective analysis and comparison, 9 rough surfaces with nominally Gaussian distributions are also generated by using the command $z = \text{normrnd}(z_{\text{ave}}, \sigma, N_x, N_y)$ in MATLAB. The average value of the surface heights is set to zero, and the standard deviation of surface heights is varied from 0.01 to 0.2 μm , which are called G1–G9. The root-mean-square (RMS) height is calculated by the following equation:

$$R_q = \sqrt{\frac{1}{N} \sum_{i=1}^N (z_i - \bar{z})^2} \tag{21}$$

where N is the total number of the measured points, z_i is the measured height at the i th point, and \bar{z} is the average height of all the measured points.

The RMS height and plasticity index are listed in Table 1. Firstly, the generated Gaussian surface G5 is used to investigate the effect of the normal force on the static friction coefficient. The rough surface plot and contour are shown in Fig. 5. and Fig. 6., respectively. Later, all the rest of the generated random surfaces are considered to investigate the effect of the plasticity index on the static friction coefficient.

3 FEM Modeling

A finite element deterministic rough surface contact model with normal and tangential loading is used to compare to the multi-scale model (description in the next section). The FEM model and the boundary conditions are shown in Fig. 7. The contact elements use the augmented LaGrange method for enforcing contact and limiting penetration between the surfaces. The augmented LaGrange method is very similar to the pure penalty method, but it adjusts the contact force with a constant that is independent of the penetration stiffness. In order to make the surface periodic, two lines are added to the last row and column, respectively, so that the heights of coordinates of points at $z(i, 1)$ and $z(i, n + 1)$, as well as $z(1, j)$ and $z(n + 1, j)$, have the same values, and they have the same displacements in the y direction. Hence, the contact surface is comprised of 129×129 nodes that results in 128×128 elements. The moving node method is employed to create the

Table 1 RMS height and plasticity index of generated Gaussian surfaces

Surface name	G1	G2	G3	G4	G5	G6	G7	G8	G9
RMS height (μm)	0.01	0.025	0.05	0.075	0.1	0.125	0.15	0.175	0.2
Plasticity index ψ	1.32	3.33	6.62	10.04	13.20	16.59	19.76	23.11	26.17

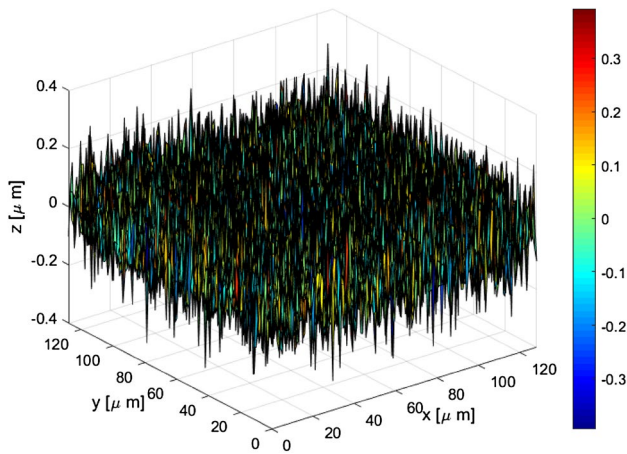


Fig. 5 Three-dimensional plot of Gaussian surface G5

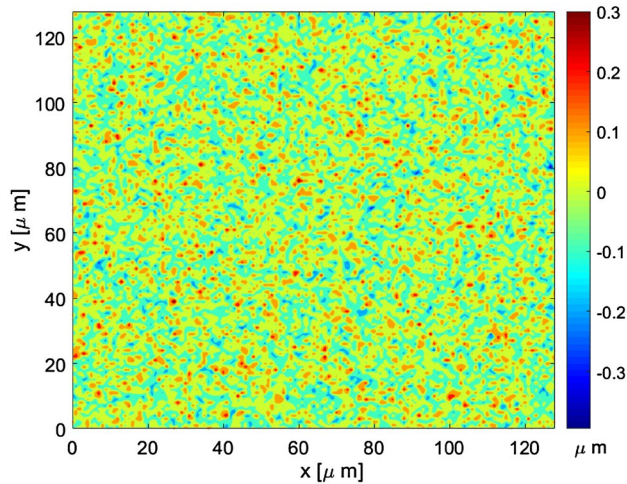


Fig. 6 Topographical contour plot of Gaussian surface G5

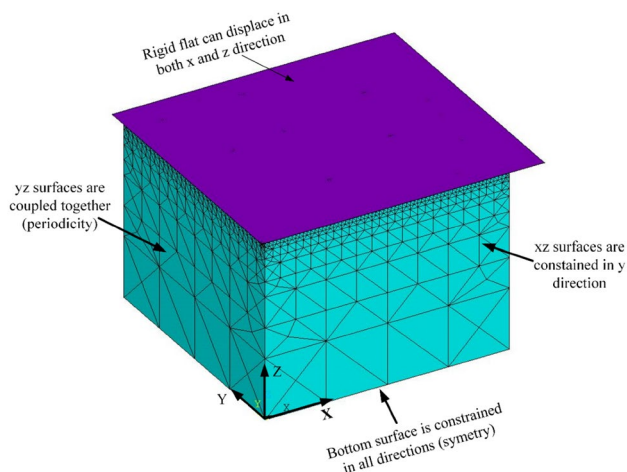


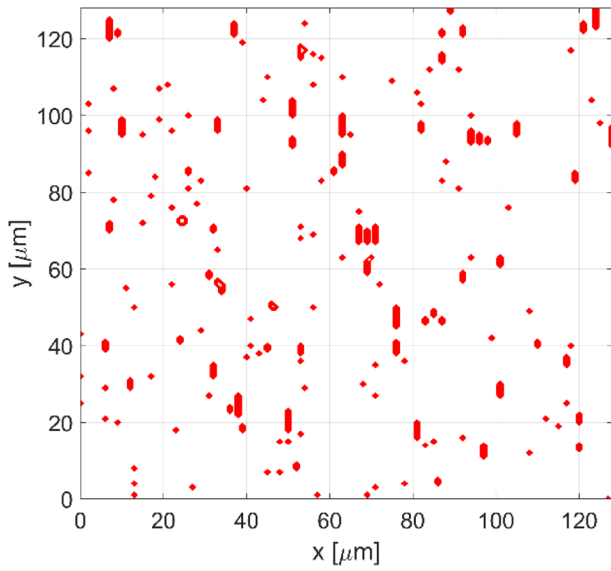
Fig. 7 Finite element model and boundary conditions for rough surface contact

rough surface geometry [44]. In order to avoid producing badly distorted elements and negative Jacobians, several steps are used to move the whole surface height from flat to rough, i.e., there are a few layers over which to apply the rough surface heights. The surface is meshed uniformly in the horizontal division. Hexahedron elements are used to model these layers, and tetrahedra elements are used to model the base. The bottom surfaces are fixed in all directions, and the xz surfaces are restrained in the y direction, and the yz surfaces on each side are coupled to enforce periodicity. The normal force is applied on the rigid flat and then the normal preload is held constant while a tangential displacement is applied on the rigid flat. The employed material properties are an elastic modulus, E , of 200 GPa, Poisson's ratio, ν , of 0.3, yield strength, S_y , of 1 GPa and a tangent modulus, E_t , of 2% of the elastic modulus. The critical interfacial shear strength, τ_c , is set to $S_y / \sqrt{3}$ (based on the von Mises yield criteria). The sliding occurs when the shear stress of all the elements reach τ_c . Then, gross sliding occurs, and the stiffness vanishes at that moment.

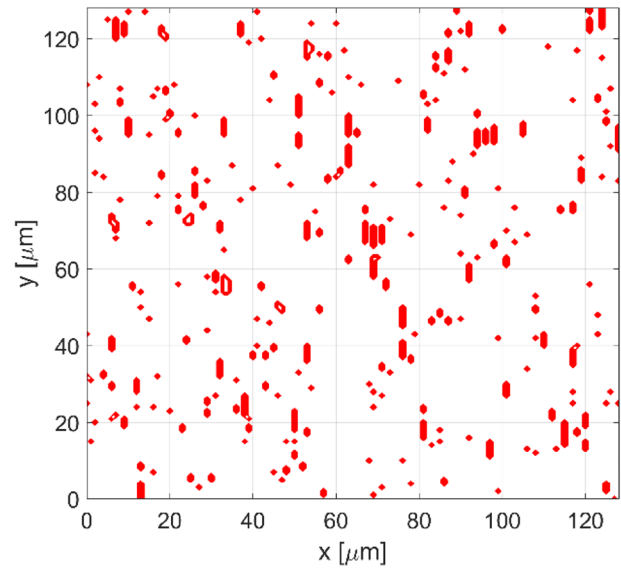
A constant normal load, F_n , was applied as a single force at the pilot node, and then, a step wide increase in the tangential displacement, u_x , of the flat was added to simulate the gradually increasing tangential load. Before tangential loading, the sinusoidal surface and the rigid flat are assumed to be in the full stick condition. Once the tangential loading is applied, the maximum frictional shear stress criterion is used for governing the local sliding initiation. The instantaneous tangential force, F_t , was obtained from the x component of the reaction at the pilot node. The sliding inception is when all the contact elements first start sliding, and the tangential force then is $(F_t)_{max}$. When this occurs the static friction coefficient is $\mu_s = (F_t)_{max} / F_n$.

The effectiveness of the FEM model is tested. The rough surface 8L is used to do the simulation. Figure 8 shows the contact area for surface 8L under the normal loads $F_n / (A_n S_y) = 0.06$ and $F_n / (A_n S_y) = 0.12$. The red color presents the local contact areas. These plots suggest that the contact area spots at this load are very small and may consist of a small number of contact elements within each asperity.

The numbers of local contact areas and contact nodes are plotted in Fig. 9. As the dimensionless normal load increases, the numbers of contact nodes increase while the number of local contact area increases until it becomes a nearly constant. Note that the results in Fig. 9 are not normalized so that the differences between them can be seen more easily. The average number of contact nodes per each local contact area (N_{pl} / N_A) as function of normalized force is plotted in Fig. 10. From Fig. 10, as the dimensionless normal load increases, the ratio increases. The ratio is below 4 for the dimensionless lower normal loads 0.06 and 0.12, i.e., there are less than 4 contact nodes for each contact area. This probably causes accuracy



(a) $F_n / (A_n S_y) = 0.06$



(b) $F_n / (A_n S_y) = 0.12$

Fig. 8 Contact area under dimensionless normal loads for surface 8L

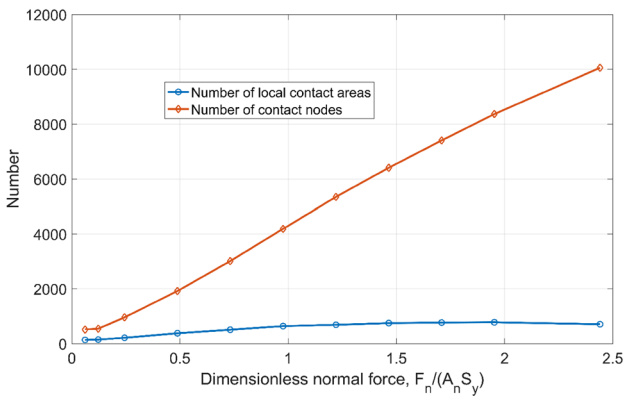


Fig. 9 Number of local contact areas and nodes versus dimensionless normal load for surface 8L

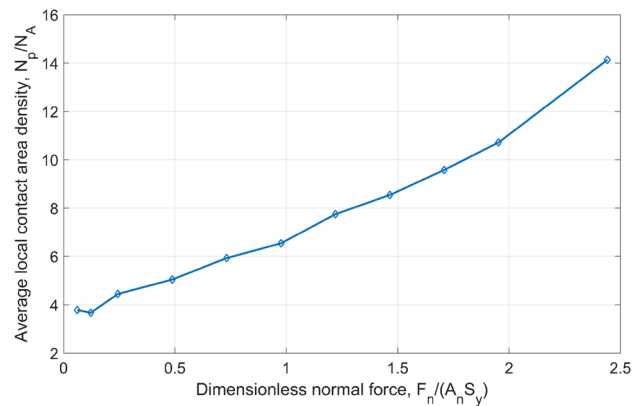


Fig. 10 Average local contact area density versus dimensionless normal force for surface 8L

problems in the FEM model. Therefore, all of the low load results are probably in error.

4 Methodology

4.1 Normally Loaded Multi-scale Model

Recall that Jackson and Streater (JS) used a stacked 3D sinusoidal geometry to represent the asperities in contact at each level of the surface, and predicted the real contact area as a function of the normal contact load. The central idea of the JS model is that a surface can be decomposed

into stacks of sinusoidal waves with different amplitudes and wavelengths, as shown in Fig. 11. Each frequency is considered a scale or layer of asperities which are stacked iteratively upon each other. The Fourier transform was used to convert the surface data into a series of stacked harmonic waves.

The basic assumptions of the JS multi-scale model [26] are: (a) Smaller asperities are located on top of the larger asperities; (b) each scale level of asperities carries the same total normal load; (c) at each scale level, all the asperities at this level share the normal load equally; (d) the contact area at a given scale level cannot be greater than the contact area at a larger scale. Note that these assumptions are not

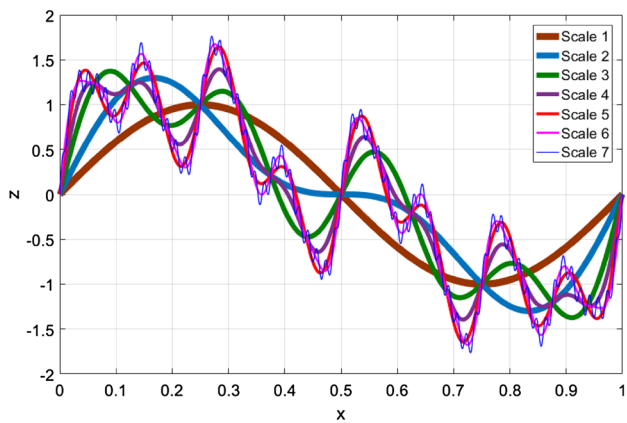


Fig. 11 A schematic depicting the decomposition of a surface into superimposed sine waves

necessarily true for a real rough surface contact, and therefore, the resulting model is an approximation, although it has shown promising comparisons to experimental results [45–47]. Based on these assumptions, each frequency level of asperities carries the same total load, and the load at each scale level is sheared equally among all the asperities at that level. Following this, the contact area is then calculated iteratively using the factorial equation:

$$A_r = \left(\prod_{i=1}^{i_{\max}} \bar{A}_i \eta_i \right) A_n \tag{22}$$

where A_r is the real area of contact, \bar{A} is the contact area of a single asperity on a certain scale of roughness, η is the real asperity density, A_n is the nominal contact area, and the subscript i denotes a specific asperity scale level, with i_{\max} denoting the smallest scale level considered.

Since each scale shares the same the total load, F_n , the contact pressure at the i th scale can be related to the total load by

$$\bar{p}_i = F_n / A_{i-1} \tag{23}$$

Where \bar{p}_i is the contact pressure at i th scale.

Each frequency level is modeled using a sinusoidal contact model, for elastic contact, The empirical equation developed by Jackson and Streator [26], which is based on the experimental data provided by Johnson et al. [48], can be used:

$$\text{For } \bar{p} < 0.8 : \quad \bar{A} = (\bar{A}_{JGH})_1 \left[1 - \left(\frac{\bar{p}}{p^*} \right)^{1.51} \right] + (\bar{A}_{JGH})_2 \left(\frac{\bar{p}}{p^*} \right)^{1.04} \tag{24}$$

$$\text{For } \bar{p} \geq 0.8 : \quad \bar{A} = (\bar{A}_{JGH})_2 \tag{25}$$

The two asymptotic solutions provided by Johnson et al. [48] are given as

$$\text{When } \bar{p} \ll p^* : \quad (\bar{A}_{JGH})_1 = \frac{\pi}{f^2} \left(\frac{3}{8\pi} \frac{\bar{p}}{p^*} \right)^{2/3} \tag{26}$$

$$\text{When } \bar{p} \rightarrow p^* : \quad (\bar{A}_{JGH})_2 = \frac{1}{f^2} \left[1 - \frac{3}{2\pi} \left(1 - \frac{\bar{p}}{p^*} \right) \right] \tag{27}$$

where p^* is the average pressure to cause complete contact between the surfaces of a single scale and is given by as:

$$p^* = \sqrt{2\pi} E' \Delta_i f_i \tag{28}$$

For elastic–plastic contact, the FEM-based equations in [49, 50] can be used.

$$\bar{A} = \bar{A}_p \left[1 - \left(\frac{\bar{p}}{p_{ep}^*} \right)^{1.51} \right] + (\bar{A}_{JGH})_2 \left(\frac{\bar{p}}{p_{ep}^*} \right)^{1.04} \tag{29}$$

where

$$\bar{A}_p = 2 \left(\frac{A_c}{2} \right)^{\frac{1}{1+d}} \left(\frac{3\bar{p}}{4CS_y} \lambda^2 \right)^{\frac{d}{1+d}} \tag{30}$$

$$d = 3.8 \left(\frac{E'}{S_y} \frac{\Delta}{\lambda} \right)^{0.11} \tag{31}$$

Ghaednia et al. [51] presented an empirical equation for the average pressure that causes complete contact for the elastic–plastic case. The equation is given as:

$$\frac{p_{ep}^*}{p^*} = 0.992 \left\{ \left(\frac{\Delta}{\Delta_c} \right)^{\left[\frac{10}{3} \left(\frac{\Delta}{\Delta_c} \right)^{-0.39} + \frac{9}{4} v^4 + 0.64 \right]} - 1 \right\} \tag{32}$$

where Δ_c is the analytically derived critical amplitude. When the amplitude is less than this value, the sinusoidal surface deforms elastically. When the amplitude is greater than this value, it deforms plastically. Δ_c is given by:

$$\Delta_c = \frac{\sqrt{2} S_y}{\pi E' f \left[3e^{-2(v+1)/3} + 2 \left(\frac{1-2v}{1-v} \right) \right]} \tag{33}$$

And $C_v C_\nu$ is a function of Poisson’s ratio and given by

$$C_v = 0.0017 \exp(8.09v) - 0.0567 \tag{34}$$

Note that when $\Delta = \Delta_c$, $p_{ep}^* = p^*$. Equation (31) results are the same overall prediction as given in [49].

4.2. Normally Loaded Multi-scale Model Results.

As discussed previously, the rough surface data set used for this model is converted into a series of stacked sine waves using the Fourier transform. All calculations for the model are then made based on the amplitude and wavelength of these sinusoidal waves.

The MATLAB command “fft2 (z, N_x, N_y)” is used to perform the Fourier transform. This command is the two-dimensional Fourier transform of a matrix using a fast Fourier transform algorithm. N_x and N_y are the number of the points in the x or y directions. In this case, N_x = N_y = N. The FFT converts the surface height matrix into a complex-valued matrix. That is, z_f = fft2 (z, N_x, N_y)/(4N²). The amplitude of the matrix can be obtained from Δ = abs(z_f) or Δ = z_f · conj(z_f). However, the method to obtain the amplitudes discussed in the Sect. 4.1 is just for a 2D profile. A single amplitude for each scale level is required, while multiple amplitudes will result from the FFT for a 3D surface. An equivalent 2D equivalent amplitude was calculated by using a two-sided amplitude spectrum method developed by Rostami and Streator [37]. A single-side spectral method is found more convenient to calculate amplitude. The equivalent amplitude can be obtained by the expression:

The wavelength can be obtained by: λ_k = L/k, where L is the scan length. For example, the wavelengths of the first and second scale level are L and L/2, respectively. The measured surface 2L is used to develop the friction model. The scan lengths in the x and y directions are both 127 μm, and the total number of points in the area is 16,384 (128 points in each direction). The resulting amplitude versus wavelength curve is plotted in Fig. 12, and the resulting amplitude to wavelength ratio versus wavelength is plotted in Fig. 13. In Fig. 13, the effective amplitude is normalized by the wavelength. The amplitude to wavelength ratio has a decreasing trend with the increasing wavelength. This trend is what is

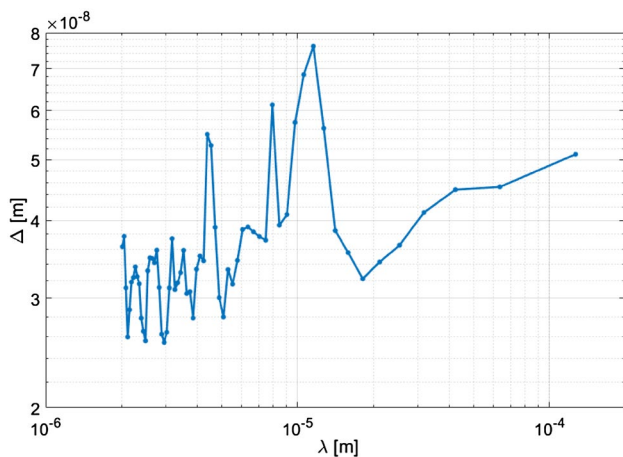


Fig. 12 Resulting amplitude versus wavelength for the surface 2L

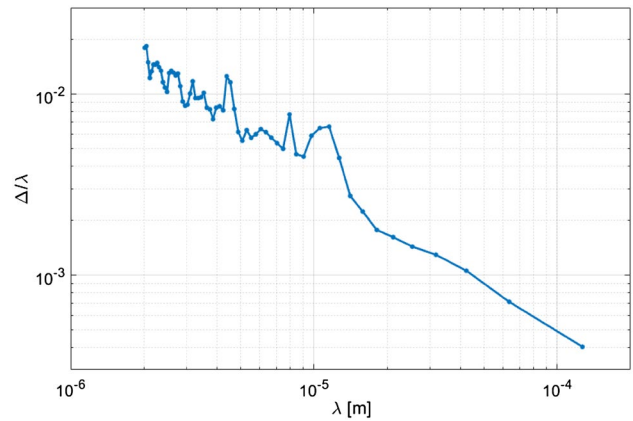


Fig. 13 Resulting amplitude/wavelength versus wavelength for the surface 2L

expected for a self-affine stochastically varying multi-scale surface structure, as discussed in Jackson [52].

Based previously on the frame work [26] discussed in Sect. 4.1, the real contact area of the rough surface can be obtained as a function of the normal load. While initially neglecting frictional load, for the elastic contact, the JGH model (Eqs. (26) and (27)) and fitted equation equations (Eqs. (24) and (25)) are used to predict the contact area on each scale level. For the elastic–plastic contact, the multi-scale framework incorporates the KJ model [50], Jackson et al. [49], and Ghaednia et al. [51] analysis to consider the asperity contact on each scale level.

In order to verify the multi-scale model, the contact area predicted by the deterministic FEM model as a function of scale level iteration under different normal loads is plotted in Fig. 14. Figure 14 shows that the scale levels cause contact area to decrease. At the same scale level, contact area increases as the dimensionless normal load increases. For

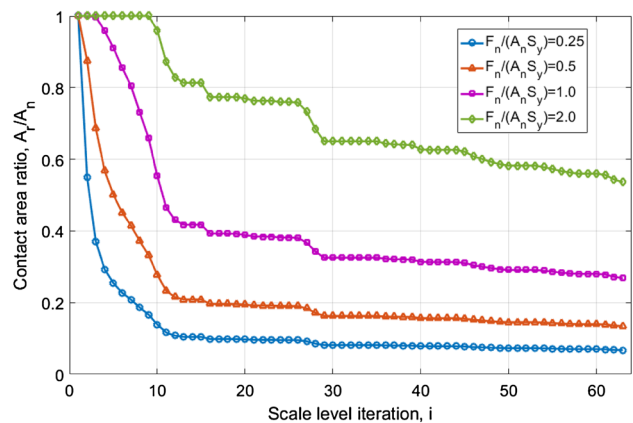


Fig. 14 Predicted contact area as a function of considered scale levels under different contact normal loads for surface 2L

the surface $2L$, the last scale to reduce contact area is at the smallest scale.

4.2 Multi-scale Static Friction Model

The following will describe how the JS multi-scale model is modified to predict the effect of tangential load and friction. The maximum shear stress criterion is used to determine the sliding inception. As discussed, when the average frictional shear stress on one asperity in contact reaches the critical interfacial shear strength, local sliding occurs. Once all the asperities in contact slide, the entire surface starts sliding.

Unlike some soft materials [53], the contact area of metallic asperities increase as the tangential load increases due to plastic deformations in the vicinity of the contact [7, 54–57], which is called junction growth. In this study, the junction growth of the rough surface can be observed in the FEM results. Figure 15 shows the junction growth of the surface $2L$ as an example. In the multi-scale friction modeling, the junction growth is considered. Therefore, the contact area at sliding inception at each scale is predicted iteratively, and the sliding contact area at sliding inception of the rough surface can be obtained.

From the FEM results, the junction growth phenomenon for this case can be observed. As can be seen from Fig. 15, as dimensionless tangential displacement increases, the contact area ratio increases and converges to a constant value at the sliding inception. For this case, the increased contact area ratio is 18.75%. Therefore, the effect of junction growth is now considered when we are building the multi-scale friction model.

To include tangential load, based on the assumptions of the normal stacked friction model, three assumptions are added:

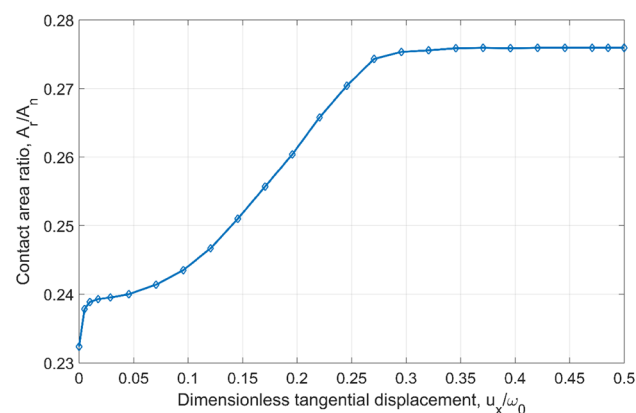


Fig. 15 FEM data of contact area evolution under combined normal and tangential loading for surface $2L$

- d. Each scale level of asperities carries the same tangential total load.
- e. At each scale level, all the asperities at this level shared the load equally.
- f. The shear stress at a given scale level cannot be less than the shear stress at a larger scale.

Note that these are limiting assumptions, but for plastic contacts the normal pressure tends to be mostly uniform and hence the load on each lateral asperity is maintained. When stacking the asperities that each scale carries, the same load is also a major assumption. It is merely based on the observation of the geometry that smaller features are usually placed on top of larger ones. These assumptions were first proposed by Archard and then later adopted by others. The assumptions have been shown in some previous works to produce a simple model that appears to work surprisingly well for contacts with plastic deformation.

To illustrate in more detail how the multi-scale friction model is used to model static friction, a flowchart is given in Fig. 16.

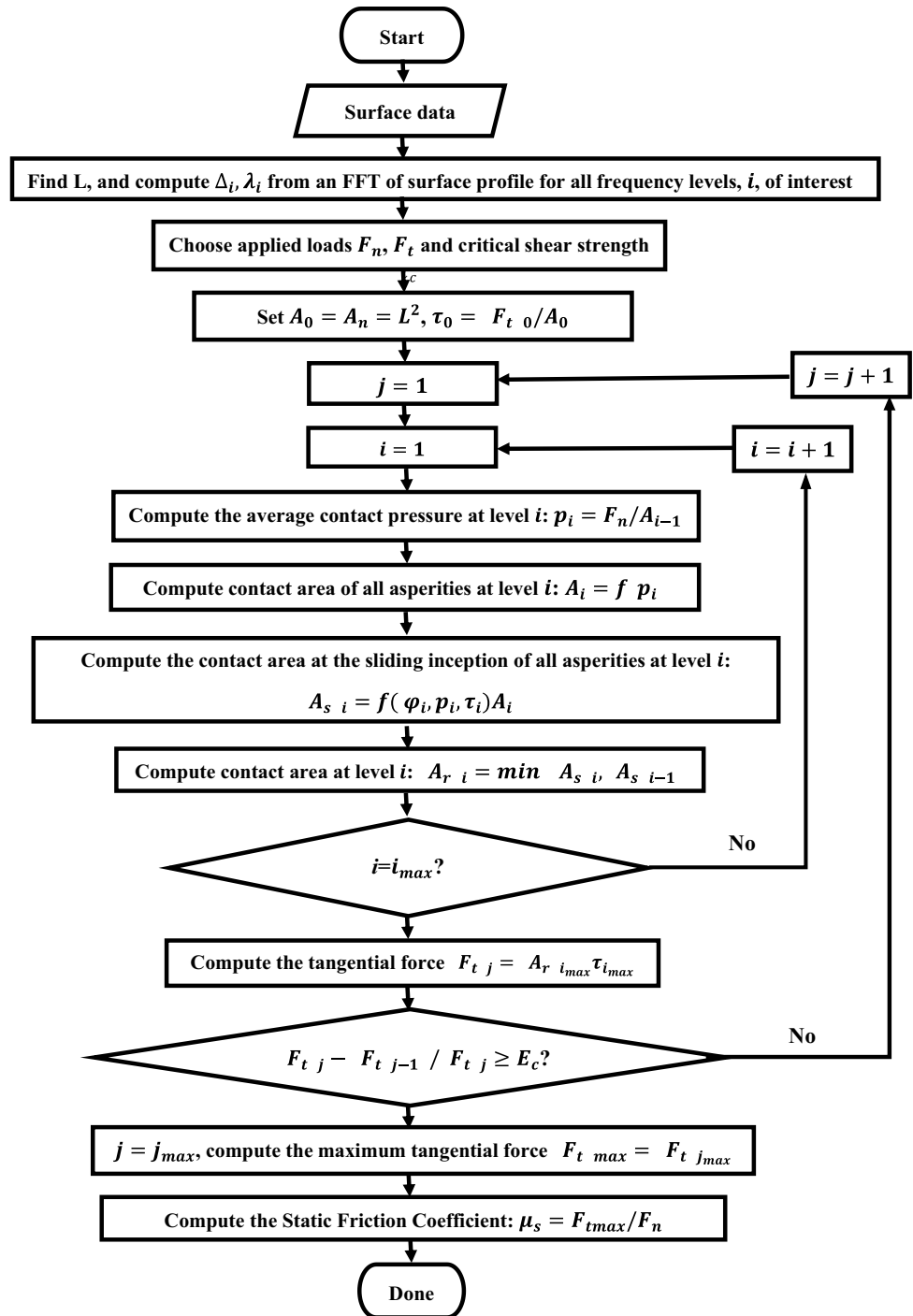
The main procedure is listed below:

- (1) Scan the rough surface and find scan length L ; then, perform an FFT from the measured data.
- (2) Calculate the parameters required at each scale level such as wavelength, λ_i , and equivalent amplitude, Δ_i , using Eq. (35). Apply a normal force, F_n .
- (3) Set the initial values: nominal contact area, A_n and critical shear strength, τ_c .
- (4) Iterate to find the maximum tangential load (i represents the scale iteration, while j represents the load iteration)

Iteration a. Apply the tangential load by several loading steps, first start iteration from $j = 1$.

Iteration b. At the first loading step, calculate the contact pressure at each scale, start iteration from $i = 1$. Considering that the total normal load is divided evenly among all the asperities of this level, compute the contact pressure applied on all the asperities at scale level 1. Compute contact area of all the asperities at level 1 under normal preload only by using Eqs. (29)–(34) for elastic–plastic contact. The contact area is determined by a given normal load, geometric parameter and set of material properties. Compute shear stress at level 1, keeping with assumption **f**, the shear stress at scale level 1 can be obtained by $\tau_1 = \max((F_t)_0/A_1, (F_t)_0/A_n)$. Considering junction growth, compute the contact area at the sliding inception, $(A_s)_1$, of each individual asperity at level 1 using:

Fig. 16 Flowchart of the proposed multi-scale friction model



$$\frac{A_s}{A_0} = 2.6 \left\{ \coth \left[15.2 \left(\frac{\bar{p}}{p_{ep}^*} \right)^{1/2} \right] \exp(-0.017 \varphi - 3) - 0.03 \varphi^{1/4} \left(\frac{\bar{p}}{p_{ep}^*} \right)^4 + 0.1364 \right\} \left[\left(\frac{\tau_c}{S_y} \right)^2 + 2.13 \right] \quad (36)$$

where the parameter φ can be expressed as:

$$\varphi = \frac{E' \Delta}{S_y \lambda} \quad (37)$$

Then, keeping with assumption **d**, guarantee that the contact area at a given scale level cannot be greater than the values of the larger scales below it. That is, choose the smaller value between the contact area at level 0 and that calculated

by Eq. 36 or $A_1 = \min((A_s)_1, A_0)$. Then, start the next iteration for $i = 2$ (increase the scale level), and calculate contact area at scale level 2 using the same procedure.

Repeat iteration until the scale number reaches i_{max} , then end iteration b.

Keeping with assumption e and assumption f, the tangential load at each scale level is the same, so it is enough to calculate the tangential force at the contacting scale, by using the real contact area times shear strength.

Start next iteration for $j = 2$ (increase the tangential load).

Repeat these procedures iteratively until the $((F_t)_j - (F_t)_{j-1}) / (F_t)_j$ is below a small constant value (E_c) to check convergence. Iteration a. ends at the j_{max} iteration.

The tangential load at the initiation of slip is the maximum tangential load that is obtained. As shown by Etsion et al. [4], the slope of the tangential load will approach zero as the maximum is approached. Therefore, the maximum tangential load at any iteration is what must be overcome to cause sliding (is static friction).

- (5) 5.) At last, compute the static friction coefficient of the rough surface, $\mu_s = (F_t)_{max} / F_n$.

5 Results and Discussion

5.1 Multi-scale Friction Model Results

Based on the procedure introduced in Sect. 4.2, the contact area is investigated first. Surface 2L under a dimensionless normal load $F_n / (A_n S_y) = 0.5$ is considered. The predicted contact areas at each scale under only normal load and at sliding inception are plotted in Fig. 17. As can be seen from

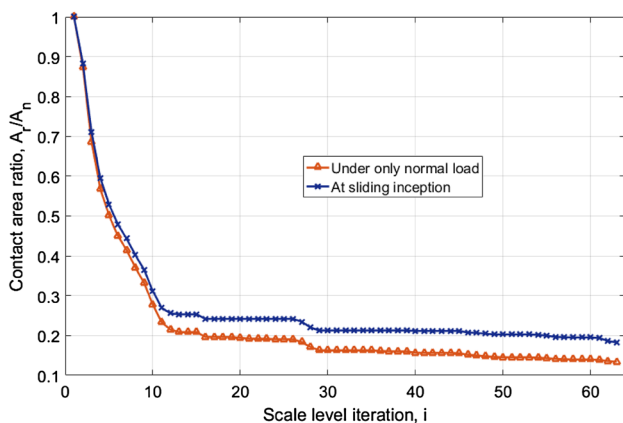


Fig. 17 Predicted static friction coefficient as a function of considered scale levels under only normal load and at sliding inception for surface 2L

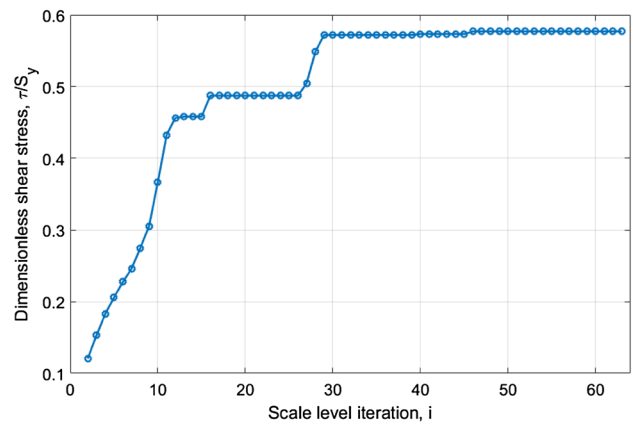


Fig. 18 Predicted shear stress as a function of considered scale levels under a dimensionless normal load $F_n / (A_n S_y) = 0.5$ for surface 2L

Fig. 17, for both cases the contact area decreases as the scale becomes smaller, and the differences between each case are due to the junction growth for each scale.

Considering assumption e, each scale level of asperities carries the same tangential total load. Then, the larger scales have smaller contact areas and lower shear stresses. The predicted shear stress is plotted in Fig. 18. The predicted shear stress increases until it reaches the critical shear strength. The larger scales have a smaller shear stress, because the tangential force is distributed over a large area. The lower scales have larger contact areas and therefore lower stresses. The increased contact area from junction growth needs more tangential force to overcome the friction. After a few iterations of increasing tangential force, the tangential force will converge to a constant value (see Fig. 19).

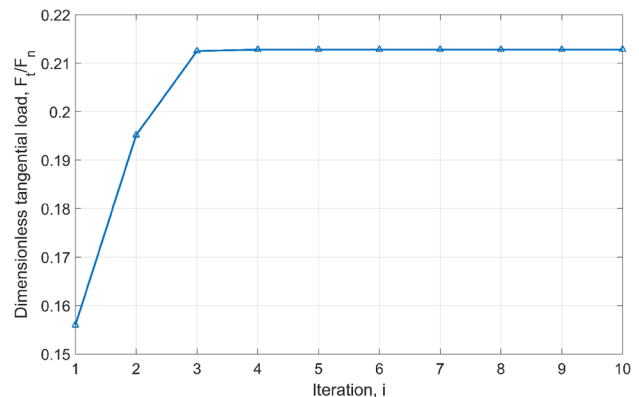


Fig. 19 Predicted dimensionless tangential load under a dimensionless normal load, $F_n / (A_n S_y) = 0.5$ for surface 2L

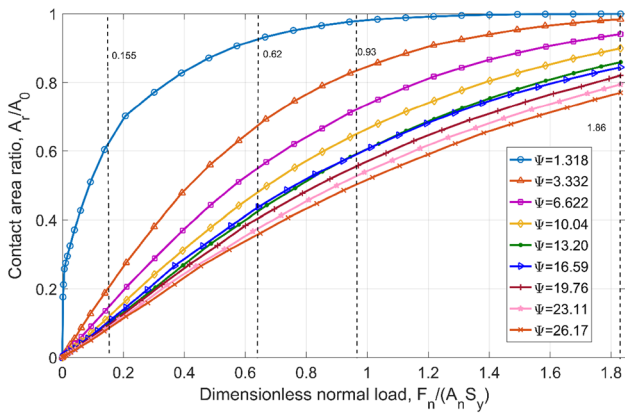


Fig. 20 Contact area ratio versus dimensionless normal load for the various surfaces with different plasticity indices

5.2 Deterministic FEM Results

In order to investigate the effect of plasticity index on the static friction coefficient, the generated Gaussian surfaces G1–G9 are used in the simulations. The contact area under only normal loading are plotted in Fig. 20. As can be seen from Fig. 20, under the same normal load, the surfaces with larger plasticity indices have lower contact area ratios in most of cases. Under the dimensionless normal load $F_n/(A_n S_y) = 1.86$, the smoothest one (surface G1) has reached complete contact ($A_r/A_n = 1$) prior to this load. The roughness is increased to increase the plasticity index. Roughness increases the amount of plastic deformation, because it also reduces the real contact area. When the real contact area is reduced, the contact pressure increases, which increases plastic deformation. Jackson and Green [58] also investigated the effect of plasticity index on the contact area ratio. They varied the

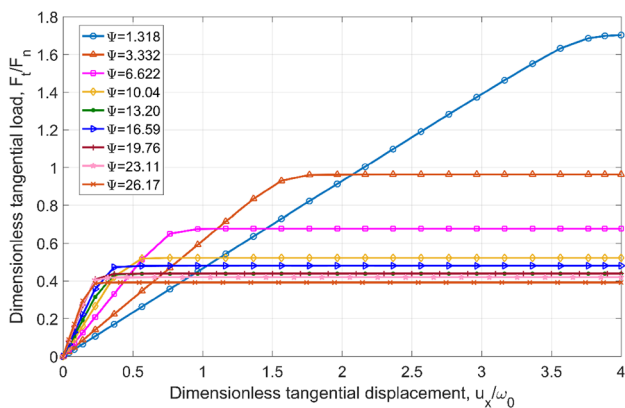


Fig. 21 Dimensionless tangential load F_t/F_n versus the dimensionless tangential displacement u_x/ω_0 for the surfaces with various plasticity indices

yield strength to vary the plasticity index while using one certain rough surface. This would increase contact area, i.e., under the same normal load, the surfaces with larger plasticity indices have larger contact area ratios. Recall from Eq. 10, the plasticity index increases as σ_s increases and while S_y decreases.

Figure 21 presents typical results for the instantaneous tangential load as a function of dimensionless tangential displacement for the surfaces with different plasticity indices. In order to show the figure clearly, the tangential displacement u_x is normalized by the interference under normal preload only, ω_0 . As shown in Fig. 21, the surfaces with higher plasticity indices have larger normalized stiffnesses, but this is only due to the normalization used. In reality, they all have nearly the same stiffness at low tangential displacements, but the stiffnesses of the higher plasticity indices decrease at lower tangential displacements. As can be seen from Fig. 21, as dimensionless tangential displacement increases dimensionless tangential load increases until it reaches a constant value for each case. At that moment, the slopes of the curves vanish and the tangential loads are the maximum tangential loads.

5.3 Comparison

5.3.1 Effect of Plasticity Index

As can be seen from Fig. 21, the tangential load at the sliding inception is the maximum tangential load $(F_t)_{max}$, which can be extracted from FEM results. The static friction coefficients are then obtained by $(F_t)_{max}/F_n$ and plotted in Fig. 22 for all the generated Gaussian surfaces. The deterministic FEM results, CKE model and LET model are also plotted in Fig. 22 to compare with the results of the proposed multi-scale model. This case

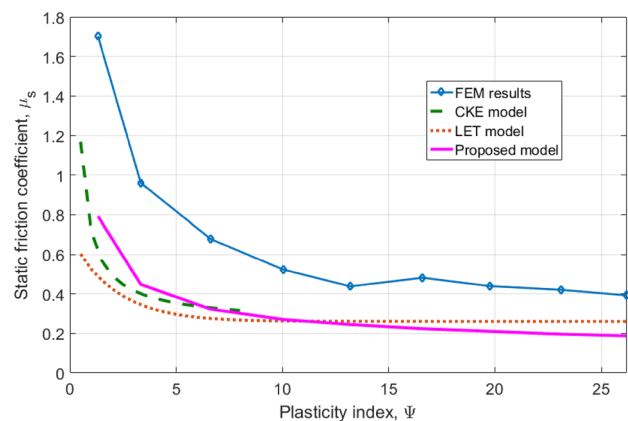


Fig. 22 Comparison of static friction coefficient for generated Gaussian surfaces with various plasticity indices under a dimensionless normal load $F_n/(A_n S_y) = 0.155$

is under the low load of ($F_n/(A_n S_y) = 0.155$). All of the models show the same trend that the static friction coefficient decreases as plasticity index increases. Note that the static friction coefficient of the surface with $\Psi = 16.59$ is higher than the static friction coefficient of the surface with $\Psi = 13.20$. Recall that the contact area of the surface with $\Psi = 16.59$ is higher than the contact area of the surface with $\Psi = 13.20$ under the same dimensionless contact pressure ($F_n/(A_n S_y) = 0.155$) (see Fig. 20). This confirms that the static friction coefficient is related to the contact area. The proposed static friction model predictions are lower than the FEM results and higher than or close to the CKE model and LET model for the surfaces with lower plasticity indices (roughly $\Psi \leq 11$). Under high loads, the static friction coefficient becomes below the LET model slightly, and it is still lower than the FEM predictions. However, the proposed multi-scale friction model predictions are less than the FEM results, especially under low normal loads.

Next, the effect of plastic index on the static friction coefficient under a heavier load $F_n/(A_n S_y) = 0.62$ is investigated. Figure 23 shows the comparison of static friction coefficient, μ_s , as a function of plasticity index, Ψ , between the proposed model and the FEM results under various normal loads for the surfaces G1 to G9. Under the normal preload $F_n/(A_n S_y) = 0.62$, the multi-scale friction model predicts lower values than the FEM data. The reason why the LET model is not compared is that it is outside of its applicable range.

Much higher loads than in Fig. 23 are also applied. The dimensionless normal preload $F_n/(A_n S_y) = 0.93$ is applied first. As can be seen from Fig. 24, the multi-scale friction model predicts lower values of the static friction coefficient than the FEM data except for the first point.

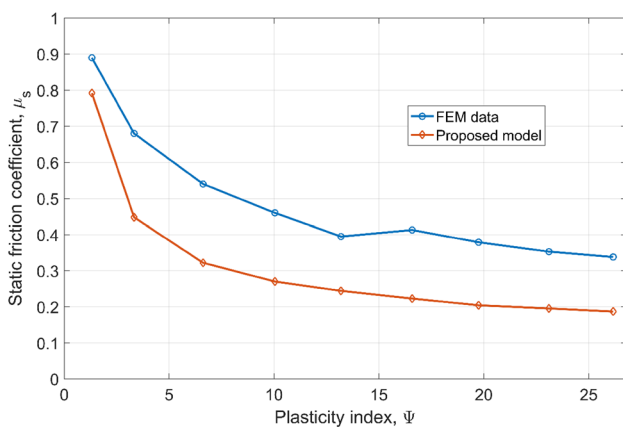


Fig. 23 Comparison of static friction coefficient between FEM data and the proposed model for surfaces with various plasticity indices under a dimensionless normal load $F_n/(A_n S_y) = 0.62$

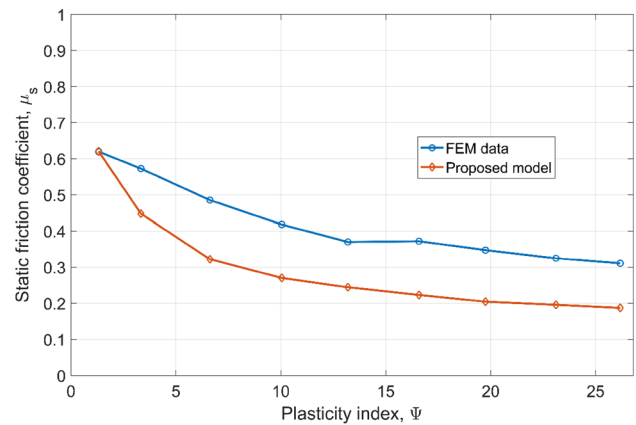


Fig. 24 Comparison of static friction coefficient between FEM data and the proposed model for surfaces with various plasticity indices under a dimensionless normal load $F_n/(A_n S_y) = 0.93$

That is because the contact area of the G1 surface under normal loading is greater than 90%, and due to junction growth the complete contact might be reached. Under the normal preload $F_n/(A_n S_y) = 1.86$, as can be seen from Fig. 25, and excluding the complete contact cases (the surfaces G1, G2 and G3 are completely flattened), the proposed static friction model predicts lower values than the FEM data. It also can be seen that as the dimensionless normal preload increases, the difference between the FEM results and proposed multi-scale model becomes smaller. Recall that the FEM data are more accurate at higher loads due to more elements in contact. In addition, the multi-scale model is also probably more accurate at higher loads, where the contact pressure is uniform due to plastic deformation.

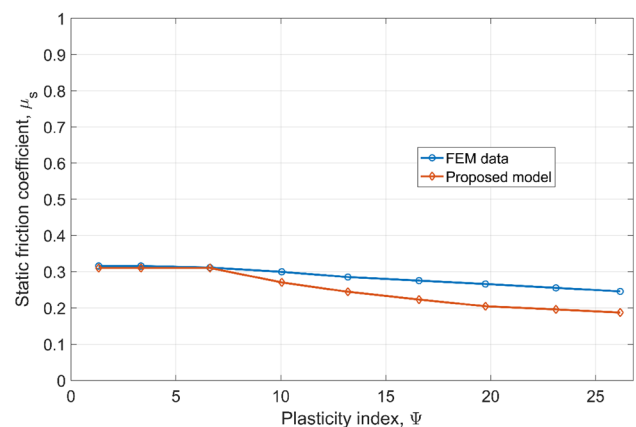


Fig. 25 Comparison of static friction coefficient between FEM data and the proposed model for surfaces with various plasticity indices under a dimensionless normal load $F_n/(A_n S_y) = 1.86$

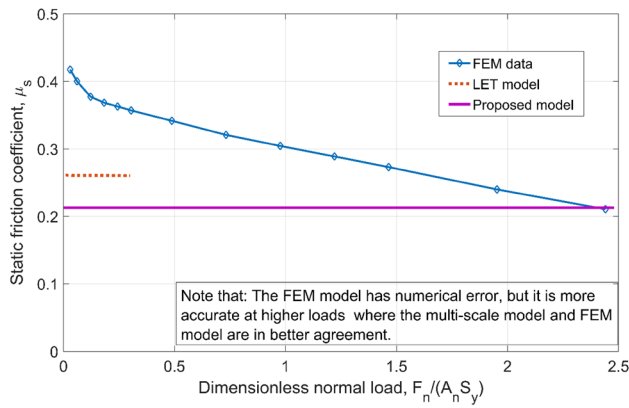


Fig. 26 Comparison of static friction coefficient between FEM results, LET model and the proposed multi-scale friction model for surface 2L

5.3.2 Effect of Normal Load

Next, the effect of normal load on the static friction model is studied. The results produced by the proposed model using the KJ model at the asperity level are compared. A comparison of the predicted static friction coefficient as a function of dimensionless normal load, $F_n/(A_n S_y)$, is made between the proposed multi-scale friction model, LET model and FEM results. As can be seen from Fig. 26, the FEM results show a decreasing trend, while the proposed model and the LET model predict a nearly constant relationship. The LET model is only valid for lower loads, as stated in the original work. As the dimensionless normal load increases, the FEM data approach the proposed model. The reason why the FEM results decrease is that it has numerical error, especially at low loads, because less elements are in contact. Therefore, it is more accurate at higher loads where it is in

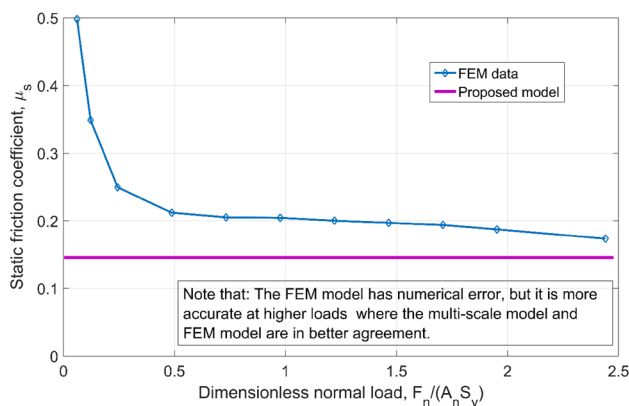


Fig. 27 Comparison of static friction coefficient between FEM results, LET model and the proposed multi-scale friction model for surface 8L

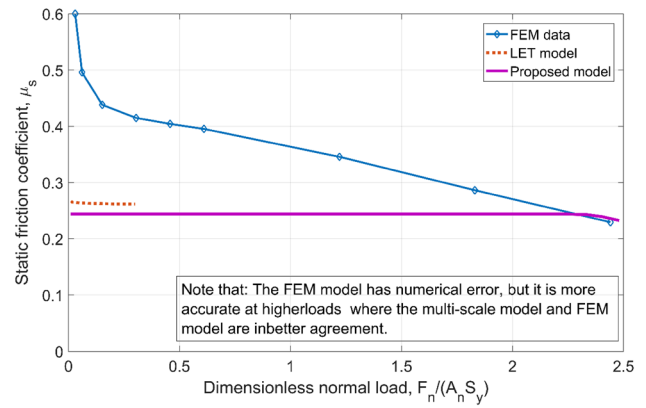


Fig. 28 Comparison of static friction coefficient between FEM results, LET model and proposed multi-scale friction model for surface G5

better agreement with the theoretical models, because then more contact elements are engaged. It should also be noted that the proposed multi-scale model also makes many limiting assumptions. Nonetheless, it is reassuring that the two models begin to agree at higher loads.

The proposed model has the same trend as the FEM model and theoretical models. There are also still some differences between them. The proposed multi-scale friction model predicts lower values than the FEM data. However, as discussed previously the proposed model is not in a good quantitative agreement with FEM results at lower loads.

The comparison between the proposed multi-scale model, FEM results and the LET model for surface 8L and G5 are plotted in Figs. 27 and 28, respectively. Interesting, both the proposed model and statistical model predict a nearly constant friction coefficient for the surface 8L and surface G5. However, one may notice that the proposed multi-scale model actually begins to curve and appear to join with the FEM results at the highest loads for surface G5 (Fig. 28). The static friction coefficients predicted by the proposed model fall below the FEM results and the LET model at low loads. They do not always show the same trend or have a good agreement. We postulate that this is mainly because the FEM model is not completely refined and that the spectral interpolation method decreases the contact area with additional refinement. However, the FEM results and proposed model predictions are fairly close under heavy normal loads, which is when the FEM model is actually most accurate.

6 Conclusion

Since most existing friction models [10, 11] have limitations on the range of normal load and plasticity: $F_n/(A_n S_y) \leq 0.3$ and $\Psi \leq 30$, a model for the static friction of rough surfaces

for a wide range of normal loads and plasticity indices was developed, which attempts to capture the multi-scale features, and elastic–plastic deformations. This study formulates an iterative multi-scale friction model framework for modeling friction between rough surfaces, which uses the Fourier series-based representation of the rough surface. A comparison of the predicted static friction coefficient between the proposed model, statistical models and FEM results was made. Note that the FEM model also has numerical error, but is more accurate at higher loads where the multi-scale model and FEM model are in better agreement.

Firstly, the effect of plasticity index on the static friction coefficient is analyzed. In this step, 9 generated Gaussian surfaces with various plasticity indices under a wide range of normal loads are used in the simulations. The proposed model shows the same trend as the theoretical models and FEM results: as the plasticity index increases, the static friction coefficient decreases. The proposed model predicts lower static friction coefficients than the FEM results, while the predictions are close to the theoretical models under high normal loads. The difference in static friction coefficients between the proposed model and FEM results becomes smaller with increasing normal load, where the FEM is more accurate.

Then, the effect of normal load on the static friction coefficient was analyzed. In this step, the surface 2L, surface 8L and surface G5 were used in the FE models. The FEM results show a decreasing trend of the static friction coefficient with load, while the proposed friction model and statistical models predict values with less variation. Again, note that the multi-scale model has limiting assumptions and that the FEM model has significant error at low loads, but is more accurate at higher loads. At higher loads, the FEM model and multi-scale model are in better agreement. The proposed model predictions are lower than the theoretical models.

Overall, the proposed model, theoretical models, and FEM results are in a good qualitative agreement, especially for higher loads and higher plasticity indices. The proposed friction model also can predict the complete contact accurately. However, the proposed model and FEM results show a big difference for the cases with lower loads and lower plasticity indices. This might be because of the numerical error in the FEM and the limiting assumptions of the multi-scale model. The FEM results are most accurate at high loads, where the results agree with multi-scale model.

7 Appendix

As shown in Fig. 21, the surfaces with higher plasticity indexes have a larger normalized tangential stiffness before reaching the sliding inception. The reason for this

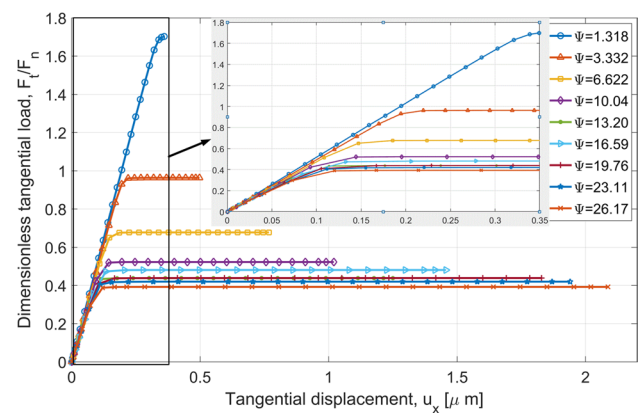


Fig. 29 Dimensionless tangential load versus tangential displacement

is the normalization. In order to show the figure clearly, the tangential displacement, is normalized by the interference under a normal preload only. The dimensionless tangential load versus tangential displacement (without normalization) is plotted in Fig. 29. The surfaces with lower plasticity index actually have larger stiffnesses, and nearly the same value at low loads, which is a different trend from Fig. 21.

References

- Kogut, L., Etsion, I.: A static friction model for elastic–plastic contacting rough surfaces. *J. Tribol.* **126**(1), 34–40 (2004). <https://doi.org/10.1115/1.1609488>
- Bowden, F.P., Bowden, T.D.: *Friction and lubrication of solids*. Clarendon, Oxford, (1954)
- Kogut, L., Etsion, I.: A semi-analytical solution for the sliding inception of a spherical contact. *J. Tribol.* **125**(3), 499–506 (2003). <https://doi.org/10.1115/1.1538190>
- Brizmer, V., Kligerman, Y., Etsion, I.: Elastic–plastic spherical contact under combined normal and tangential loading in full stick. *Tribol. Lett.* **25**(1), 61–70 (2007)
- Eriten, M., Polycarpou, A.A., Bergman, L.A.: Physics-based modeling for partial slip behavior of spherical contacts. *Int. J. Solids Struct.* **47**(18–19), 2554–2567 (2010). <https://doi.org/10.1016/j.ijsolstr.2010.05.017>
- Wu, A.Z., Shi, X., Polycarpou, A.A.: An Elastic–plastic spherical contact model under combined normal and tangential loading. *J. Appl. Mech.* **79**(5) (2012). <https://doi.org/10.1115/1.4006457>
- Wang, X., Xu, Y., Jackson, R.L.: Elastic–Plastic sinusoidal waviness contact under combined normal and tangential loading. *Tribol Lett* **65**(2), 45 (2017)
- Chang, W.R., Etsion, I., Bogy, D.B.: Static friction coefficient model for metallic rough surfaces. *J. Tribol.* **110**(1), 57–63 (1988)
- Kogut, L., Etsion, I.: A finite element based elastic–plastic model for the contact of rough surfaces. *Tribol. T.* **46**(3), 383–390 (2003). doi:<https://doi.org/10.1080/10402000308982641>
- Cohen, D., Kligerman, Y., Etsion, I.: A model for contact and static friction of nominally flat rough surfaces under full stick contact condition. *J. Tribol.* **130**(3) (2008). <https://doi.org/10.1115/1.2908925>
- Li, L., Etsion, I., Talke, F.E.: Contact area and static friction of rough surfaces with high plasticity index. *J. Tribol.* **132**(3) (2010). <https://doi.org/10.1115/1.4001555>

12. Greenwood, J., Williamson, J.P.: Contact of nominally flat surfaces. In: Proceedings of the Royal Society of London A: Mathematical, Physical and Engineering Sciences 1966, pp. 300–319. The Royal Society
13. Etsion, I., Amit, M.: The effect of small normal loads on the static friction coefficient for very smooth surfaces. *J. Tribol.* **115**(3), 406–410 (1993). doi:<https://doi.org/10.1115/1.2921651>
14. Cohen, D., Kligerman, Y., Etsion, I.: The effect of surface roughness on static friction and junction growth of an elastic-plastic spherical contact. *J. Tribol.* **131**(2) (2009). <https://doi.org/10.1115/1.3075866>
15. Meccool, J.L.: Relating profile instrument measurements to the functional performance of rough surfaces. *J. Tribol.* **109**(2), 264–270 (1987)
16. Jackson, R.L., Green, I.: A finite element study of elasto-plastic hemispherical contact against a rigid flat. *J. Tribol.* **127**(2), 343–354 (2005). <https://doi.org/10.1115/1.1866166>
17. Kogut, L., Jackson, R.L.: A comparison of contact modeling utilizing statistical and fractal approaches. *J. Tribol.* **128**(1), 213–217 (2006). doi:<https://doi.org/10.1115/1.2114949>
18. Jackson, R.L., Green, I.: On the modeling of elastic contact between rough surfaces. *Trib. Trans.* **54**(2), 300–314 (2011)
19. Tayebi, N., Polycarpou, A.A.: Modeling the effect of skewness and kurtosis on the static friction coefficient of rough surfaces. *Tribol. Int.* **37**(6), 491–505 (2004). <https://doi.org/10.1016/j.triboint.2003.11.010>
20. Lee, C.H., Polycarpou, A.A.: Static friction experiments and verification of an improved elastic-plastic model including roughness effects. *J. Tribol.* **129**(4), 754–760 (2007). <https://doi.org/10.1115/1.2768074>
21. Lee, C.H., Eriten, M., Polycarpou, A.A.: Application of elastic-plastic static friction models to rough surfaces with asymmetric asperity distribution. *J. Tribol.* **132**(3), 031602 (2010). <https://doi.org/10.1115/1.4001547>
22. Dickey, R.D.I., Jackson, R.L., Flowers, G.T.: Measurements of the static friction coefficient between tin surfaces and comparison to a theoretical model. *J. Tribol.* **133**(3), 031408 (2011). <https://doi.org/10.1115/1.4004338>
23. Archard, J.: Elastic deformation and the laws of friction. In: Proceedings of the Royal Society of London A: Mathematical, Physical and Engineering Sciences 1957, pp. 190–205. The Royal Society (1957)
24. Ciavarella, M., Demelio, G., Barber, J.R., Jang, Y.H.: Linear elastic contact of the Weierstrass profile. *Proc. Royal Soc. A* **456**, 387–405 (2000). <https://doi.org/10.1098/rspa.2000.0522>
25. Westergaard, H.M.: Bearing pressures and cracks. *Journal of Applied Mechanics-Transactions of the Asme* **6**, 49–53 (1939)
26. Jackson, R.L., Streater, J.L.: A multi-scale model for contact between rough surfaces. *Wear* **261**(11–12), 1337–1347 (2006). <https://doi.org/10.1016/j.wear.2006.03.015>
27. Gao, Y.F., Bower, A.F.: Elastic-plastic contact of a rough surface with Weierstrass profile. *Proc. Royal Soc. A* **462**(2065), 319–348 (2006). <https://doi.org/10.1098/rspa.2005.1563>
28. Wilson, W.E., Angadi, S.V., Jackson, R.L.: Surface separation and contact resistance considering sinusoidal elastic-plastic multi-scale rough surface contact. *Wear* **268**(1), 190–201 (2010)
29. Pastewka, L., Robbins, M.O.: Contact between rough surfaces and a criterion for macroscopic adhesion. *Proc. Natl. Acad. Sci. USA* **111**(9), 3298–3303 (2014). <https://doi.org/10.1073/pnas.1320846111>
30. Polonsky, I.A., Keer, L.M.: Fast methods for solving rough contact problems: a comparative study. *J. Tribol.* **122**(1), 36–41 (2000). doi:<https://doi.org/10.1115/1.555326>
31. Yang, C., Persson, B.N.J., Israelachvili, J., Rosenberg, K.: Contact mechanics with adhesion: interfacial separation and contact area. *Europhys. Lett.* **84**(4) (2008). <https://doi.org/10.1209/0295-5075/84/46004>
32. Persson, B.N.J., Scaraggi, M.: Theory of adhesion: role of surface roughness. *J. Chem. Phys.* **141**(12) (2014). <https://doi.org/10.1063/1.4895789>
33. Wu, J.J.: Numerical analyses on elliptical adhesive contact. *J. Phys. D* **39**(9), 1899–1907 (2006). <https://doi.org/10.1088/0022-3727/39/9/027>
34. Ilincic, S., Vernes, A., Vorlauffer, G., Hunger, H., Dorr, N., Franek, F.: Numerical estimation of wear in reciprocating tribological experiments. *Proc. Inst. Mech. Eng. J* **227**(J5), 510–519 (2013). <https://doi.org/10.1177/1350650113476606>
35. Solhjoo, S., Vakis, A.I.: Continuum mechanics at the atomic scale: Insights into non-adhesive contacts using molecular dynamics simulations. *J. Appl. Phys.* **120**(21) (2016). <https://doi.org/10.1063/1.4967795>
36. Rostami, A., Jackson, R.L.: Predictions of the average surface separation and stiffness between contacting elastic and elastic-plastic sinusoidal surfaces. *Proc. Inst. Mech. Eng. J* **227**(12), 1376–1385 (2013). <https://doi.org/10.1177/1350650113495188>
37. Rostami, A., Streater, J.L.: Study of liquid-mediated adhesion between 3D rough surfaces: a spectral approach. *Tribol. Int.* **84**, 36–47 (2015)
38. Medina, S., Dini, D.: A numerical model for the deterministic analysis of adhesive rough contacts down to the nano-scale. *Int. J. Solids Struct.* **51**(14), 2620–2632 (2014). <https://doi.org/10.1016/j.ijsolstr.2014.03.033>
39. Putignano, C., Afferrante, L., Carbone, G., Demelio, G.: A new efficient numerical method for contact mechanics of rough surfaces. *Int. J. Solids Struct.* **49**(2), 338–343 (2012). <https://doi.org/10.1016/j.ijsolstr.2011.10.009>
40. Afferrante, L., Carbone, G., Demelio, G.: Interacting and coalescing Hertzian asperities: a new multiasperity contact model. *Wear* **278**, 28–33 (2012). <https://doi.org/10.1016/j.wear.2011.12.013>
41. Muser, M.H., Dapp, W.B., Bugnicourt, R., Sainsot, P., Lesaffre, N., Lubrecht, T.A., Persson, B.N.J., Harris, K., Bennett, A., Schulze, K., Rohde, S., Ifju, P., Sawyer, W.G., Angelini, T., Esfahani, H.A., Kadkhodaei, M., Akbarzadeh, S., Wu, J.J., Vorlauffer, G., Vernes, A., Solhjoo, S., Vakis, A.I., Jackson, R.L., Xu, Y., Streater, J., Rostami, A., Dini, D., Medina, S., Carbone, G., Bottiglione, F., Afferrante, L., Monti, J., Pastewka, L., Robbins, M.O., Greenwood, J.A.: Meeting the contact-mechanics challenge. *Tribol. Lett.* **65**(4) (2017). <https://doi.org/10.1007/S11249-017-0900-2>
42. Ning, Y., Polycarpou, A.A.: Extracting summit roughness parameters from random Gaussian surfaces accounting for asymmetry of the summit heights. *J. Tribol.* **126**(4), 761–766 (2004). <https://doi.org/10.1115/1.1792698>
43. Yu, N., Polycarpou, A.A.: Combining and contacting of two rough surfaces with asymmetric distribution of asperity heights. *J. Tribol.* **126**(2), 225–232 (2004). <https://doi.org/10.1115/1.1614822>
44. Xu, Y.: An analysis of elastic rough contact models. (2012)
45. Jackson, R.L., Bhavnani, S.H., Ferguson, T.P.: A multi-scale model of thermal contact resistance between rough surfaces. *ASME J. Heat Transfer* **130**, 081301 (2008)
46. Jackson, R.L., Ghaednia, H., Elkady, Y.A., Bhavnani, S.H., Knight, R.W.: A closed-form multiscale thermal contact resistance model. *IEEE Trans. Compon. Packag. Manuf. Technol.* **2**(7), 1158–1171 (2012)
47. Almeida, L., Ramadoss, R., Jackson, R., Ishikawa, K., Yu, Q.: Laterally actuated multicontact MEMS relay fabricated using MetalMUMPS process: experimental characterization and multi-scale contact modeling. *J. Micro/Nanolith. MEMS MOEMS* **6**(2), 023009 (2007)
48. Johnson, K.L., Greenwood, J.A., Higginson, J.G.: The contact of elastic regular wavy surfaces. *Int. J. Mech. Sci.* **27**(6), 383 (1985). doi:[https://doi.org/10.1016/0020-7403\(85\)90029-3](https://doi.org/10.1016/0020-7403(85)90029-3)

49. Jackson, R.L., Krithivasan, V., Wilson, W.E.: The pressure to cause complete contact between elastic-plastic sinusoidal surfaces. *Proc. Inst. Mech. Eng. J* **222**(J7), 857–863 (2008). <https://doi.org/10.1243/13506501JET429>
50. Krithivasan, V., Jackson, R.L.: An analysis of three-dimensional elasto-plastic sinusoidal contact. *Tribol. Lett.* **27**(1), 31–43 (2007). <https://doi.org/10.1007/s11249-007-9200-6>
51. Ghaednia, H., Wang, X., Saha, S., Jackson, R.L., Xu, Y., Sharma, A.: A Review of elastic-plastic contact mechanics. *Appl. Mech. Rev.* **69**(6), 060804 (2017)
52. Jackson, R.L.: An analytical solution to an archard-type fractal rough surface contact model. *Tribol. T.* **53**(4), 543–553 (2010). <https://doi.org/10.1080/10402000903502261>
53. Sahli, R., Pallares, G., Ducottet, C., Ali, B., Al Akhrass, I.E., Guibert, S., Scheibert, M.: J.: Evolution of real contact area under shear and the value of static friction of soft materials. *Proc. Natl. Acad. Sci. USA.* **115**(3), 471–476 (2018). <https://doi.org/10.1073/pnas.1706434115>
54. Ovcharenko, A., Halperin, G., Etsion, I., Varenberg, M.: A novel test rig for in situ and real time optical measurement of the contact area evolution during pre-sliding of a spherical contact. *Tribol. Lett.* **23**(1), 55–63 (2006). <https://doi.org/10.1007/s11249-006-9113-9>
55. Brizmer, V., Kligerman, Y., Etsion, I.: A model for junction growth of a spherical contact under full stick condition. *J. Tribol.* **129**(4), 783–790 (2007). <https://doi.org/10.1115/1.2772322>
56. Ovcharenko, A., Halperin, G., Etsion, I.: In situ and real-time optical investigation of junction growth in spherical elastic-plastic contact. *Wear.* **264**(11–12), 1043–1050 (2008). <https://doi.org/10.1016/j.wear.2007.08.009>
57. Zolotarevskiy, V., Kligerman, Y., Etsion, I.: The evolution of static friction for elastic-plastic spherical contact in pre-sliding. *J. Tribol.* **133**(3) (2011). <https://doi.org/10.1115/1.4004304>
58. Jackson, R.L., Green, I.: A statistical model of elasto-plastic asperity contact between rough surfaces. *Tribol. Int.* **39**(9), 906–914 (2006). <https://doi.org/10.1016/j.triboint.2005.09.001>